A&A 656, A104 (2021)
https://doi.org/10.1051/0004-6361/202141516

Astronomy & Astrophysics

Reconstructing solar irradiance from historical Ca II K observations

I. Method and its validation

Theodosios Chatzistergos[1,2], Natalie A. Krivova[1], Ilaria Ermolli[2], Kok Leng Yeo[1], Sudip Mandal[1], Sami K. Solanki[1,3], Greg Kopp[4], and Jean-Marie Malherbe[5,6]

[1] Max Planck Institute for Solar System Research, Justus-von-Liebig-Weg 3, 37077 Göttingen, Germany
e-mail: chatzistergos@mps.mpg.de
[2] INAF Osservatorio Astronomico di Roma, Via Frascati 33, 00078 Monte, Porzio Catone, Italy
[3] School of Space Research, Kyung Hee University, Yongin, Gyeonggi 446-701, Republic of Korea
[4] Laboratory for Atmospheric and Space Physics, University of Colorado Boulder, Boulder, CO, USA
[5] LESIA, Observatoire de Paris, 92195 Meudon, France
[6] PSL Research University, Paris, France

Received 10 June 2021 / Accepted 13 September 2021

ABSTRACT

Context. Knowledge of solar irradiance variability is critical to Earth's climate models and understanding the solar influence on Earth's climate. Direct solar irradiance measurements have only been available since 1978. Reconstructions of past variability typically rely on sunspot data. However, sunspot records provide only indirect information on the facular and network regions, which are decisive contributors to irradiance variability on timescales of the solar cycle and longer.
Aims. Our ultimate goal is to reconstruct past solar irradiance variations using historical full-disc Ca II K observations to describe the facular contribution independently of sunspot observations. Here, we develop the method and test it extensively by using modern CCD-based (charge-coupled device) Ca II K observations. We also carry out initial tests on two photographic archives.
Methods. We employ carefully reduced and calibrated Ca II K images from 13 datasets, including some of the most prominent series, such as those from the Meudon, Mt Wilson, and Rome observatories. We convert them to unsigned magnetic field maps and then use them as input to the adapted Spectral and Total Irradiance Reconstruction (SATIRE) model to reconstruct total solar irradiance (TSI) variations over the period 1978–2019, for which direct irradiance measurements are available.
Results. The reconstructed irradiance from the analysed Ca II K archives agrees well with direct irradiance measurements and existing reconstructions. The model also returns good results on data taken with different bandpasses and images with low spatial resolution. Historical Ca II K archives suffer from numerous inconsistencies, but we show that these archives can still be used to reconstruct TSI with reasonable accuracy provided the observations are accurately processed and the effects of changes in instrumentation and instrumental parameters are identified and accounted for. The reconstructions are relatively insensitive to the TSI reference record used to fix the single free parameter of the model. Furthermore, even employment of a series, itself reconstructed from Ca II K data, as a reference for further reconstructions returns nearly equally accurate results. This will enable the Ca II K archives without an overlap with direct irradiance measurements to be used to reconstruct past irradiance.
Conclusions. By using the unsigned magnetic maps of the Sun reconstructed from modern high-quality Ca II K observations as input into the SATIRE model, we can reconstruct solar irradiance variations nearly as accurately as from directly recorded magnetograms. Historical Ca II K observations can also be used for past irradiance reconstructions but need additional care, for example identifying and accounting for discontinuities and changes in the quality of the data with time.

Key words. Sun: activity – Sun: photosphere – Sun: chromosphere – Sun: faculae, plages – solar-terrestrial relations

1. Introduction

The Sun is the dominant energy source of Earth's system (Kren et al. 2017) and is thus one of the main natural drivers of Earth's climate. However, the mechanisms of this forcing are not yet fully understood, due to the complex dynamics of the climate system and the scarcity of appropriate solar data (e.g., Haigh 2007; Gray et al. 2010; Ermolli et al. 2013; Solanki et al. 2013; Krivova 2018).

Climate models require information on past changes in the solar irradiance (Intergovernmental Panel on Climate Change 2013, 2021; Matthes et al. 2017), which is the solar radiative energy flux per unit area as measured at the top of the Earth's atmosphere at a mean Sun-Earth distance of one astronomical unit. The solar irradiance integrated over the entire spectrum, called the total solar irradiance (TSI), describes the total solar energy input and has been measured nearly continuously since 1978 by various radiometers from space (e.g., Hickey et al. 1980; Willson & Hudson 1988; Fröhlich et al. 1997; Kopp et al. 2005; Schmutz et al. 2013; Pilewskie et al. 2018). These measurements show that the TSI varies at all discernible timescales from minutes to decades, the most distinctive being a clear ~0.1% change in phase with the solar cycle (Fröhlich 2013; Kopp 2016). There is also indirect evidence for longer-term irradiance changes, which are of primary interest to climate studies. Since no irradiance measurements are available for

the period prior to 1978, models are used to reconstruct past variations.

It has been demonstrated that the main driver of the irradiance variability on timescales of days to decades is the perpetual competition between the dark and bright magnetic regions emerging through the solar surface (see e.g., Foukal et al. 1977; Yeo et al. 2017b; Shapiro et al. 2017, and references therein), that is the dark sunspots and the bright faculae and network (hereafter collectively referred to as faculae) seen in white light in the photosphere. Thus, models have been developed that reconstruct solar irradiance changes by accounting for sunspot darkening and facular brightening. The most successful models reproduce over 90% of the measured TSI variability (e.g., Krivova et al. 2003; Chapman et al. 2013; Yeo et al. 2014, 2017a,b; Dasi-Espuig et al. 2016; Lean 2018; Wu et al. 2018; Chatzistergos et al. 2020a). The success of these models suggests that it is possible to reconstruct past irradiance variability, provided the contributions by spots and faculae are known.

The compiled series of counts of sunspots (the sunspot number) and their groups (the group sunspot number) go back to 1700 and 1609, respectively, and have been most widely used for irradiance reconstructions extending back to the Maunder Minimum. As with most historical data, they are not free of problems. In particular, the cross-calibration of records by individual observers has recently been debated (Clette & Lefèvre 2016, 2018; Lockwood et al. 2016; Usoskin et al. 2016a). This led to the development of new techniques (Usoskin et al. 2016b; Willamo et al. 2017; Chatzistergos et al. 2017), reanalysis of some data, and the recovery of additional sources (e.g., Arlt et al. 2013, 2016; Vaquero et al. 2016; Carrasco et al. 2018, 2019, 2021a,b; Hayakawa et al. 2020a,b, 2021; Vokhmyanin et al. 2020), which improved the accuracy of the sunspot number records and thus irradiance reconstructions (Kopp et al. 2016).

More critical for historical reconstructions, however, is the lack of accurate information on the evolution of faculae and the network. This is particularly unfortunate as changes in the network are believed to be the main source of the secular irradiance variability (Solanki et al. 2002), which is the prime interest of climate studies. Various models take different roundabout approaches to estimate the possible changes in the facular component in the past. Thus, estimates of the change in TSI since the Maunder Minimum reported in the literature diverge by about an order of magnitude (see e.g., Solanki et al. 2013; cf. Yeo et al. 2020).

Historical solar observations in the Ca II K line have the unique potential of providing information on the evolution of faculae (or plage as they are called when seen in the chromosphere). Such observations started at the end of the 19th century and multiple observatories around the globe have initiated related programmes. The established link between the Ca II K brightness and photospheric magnetic field strength in bright magnetic regions (e.g., Babcock & Babcock 1955; Skumanich et al. 1984; Schrijver et al. 1989; Loukitcheva et al. 2009; Kahil et al. 2017, 2019; Chatzistergos et al. 2019d) make these data an excellent proxy of solar magnetic activity.

Ca II K observations have, indeed, been used for irradiance modelling in the past. Table 1 lists published models that employed Ca II K data for irradiance reconstructions. Most of these models employed disc-integrated measurements of plage areas derived from analysis of a single modern archive of Ca II K observations taken with charge-coupled devices (CCD) and were limited to the last several decades. Typically, such models combine the plage area series with a sunspot record (number or areas) through a linear regression to match a record of irradiance measurements (see the first block of Table 1). Another group of models followed the approach first used by Johannesson et al. (1995) and Chapman et al. (1996), who considered the disc-integrated intensity in the Ca II K line as a facular proxy. Johannesson et al. (1995) used only Ca II K data, while Chapman et al. (1996) used a disc-integrated intensity time series produced from observations in the red (672.3 nm) continuum as a sunspot proxy in addition to the Ca II K data (see second block of Table 1). The more advanced semi-empirical models (last block of Table 1) employed the modern CCD observations to derive the locations of various magnetic regions on the surface. They then used the appropriate semi-empirical solar model atmospheres for these various features to assign the corresponding intensity spectrum to each pixel of the image. The brightness of all pixels is then summed up to give the irradiance. A similar approach was applied by Morrill (2005) and Morrill et al. (2011b) to reconstruct the irradiance around the Mg II line (276–288 nm) but they used empirical centre-to-limb (CLV, hereafter) functions derived from HRTS-9 (High Resolution Telescope and Spectrograph; Brueckner & Bartoe 1983) rocket observations instead of semi-empirical model atmospheres. Thus, this approach could only be used at the wavelengths where the CLVs were obtained.

To our knowledge, only three published TSI reconstructions are based on historical Ca II K photographic observations, all from Mt Wilson, and extend beyond the direct TSI measurements, going as far back as 1915 (Foukal 2002, 2012; Ambelu et al. 2011). They used a regression model with disc-integrated plage area series or Ca II K index as facular proxy. The series employed were derived from raw digitised images of the historical photographic observations without accounting for the problems plaguing such data (see Chatzistergos et al. 2018b, 2019b). Therefore, no meaningful conclusion can be drawn about the secular irradiance variability from this analysis.

To fill this gap and ultimately reconstruct solar irradiance from direct facular observations over a period longer than several decades, we started a comprehensive action on collecting and processing the available historical Ca II K data to bring them into the form needed to achieve more reliable irradiance reconstructions. Chatzistergos et al. (2018b) developed a new method to accurately process historical and modern Ca II K observations. By applying this method on synthetic data, Chatzistergos et al. (2018b, 2019b) showed that it performs significantly better than other published methods. In subsequent studies we collected and processed numerous archives of Ca II K observations covering the period 1892–2019 (Chatzistergos et al. 2016, 2018a,b, 2019a,b,c, 2020b,c). Furthermore, using a large sample of high-quality near co-temporal modern observations in Ca II K and magnetograms, Chatzistergos et al. (2019d) reassessed the relation between Ca II K brightness and magnetic field strength. This allows a reconstruction of maps of the unsigned magnetic field strength from Ca II K observations with the accuracy required for irradiance reconstructions.

Here we take the next step and reconstruct TSI variations over the period 1978–2019 with the Spectral And Total Irradiance Reconstructions model (SATIRE, Fligge et al. 2000; Krivova et al. 2003; Yeo et al. 2014) adapted to exploit modern and historical Ca II K observations. The model and the data are described in Sects. 2 and 3, respectively. In Sect. 4 we present the reconstruction from modern data, while in Sect. 5 we test the effect of some potential problems typical of historical data (such as variations in bandwidth, central wavelength, seeing as well as instrumental changes) on the quality of the reconstructions. Finally, we summarise our results and draw conclusions in Sect. 6.

Table 1. Studies that reconstructed solar irradiance by using Ca II K observations.

Study	Ca II K data		Years	Spectral range
	Type	Archive		[nm]
Empirical models				
Oster et al. (1982)	Disc-integrated plage area	MW	1980	TSI
Schatten et al. (1985)	Disc-integrated plage area	MW	1978–1982	TSI
Foukal & Lean (1986)	Disc-integrated plage area	MW	1978–1982	TSI
Foukal & Lean (1988)	Disc-integrated plage area	MW	1978–1984	TSI
Lean & Skumanich (1983)	Disc-integrated plage area	MW	1969–1980	121.57
Lean & Repoff (1987)	Disc-integrated plage area	MW	1978–1982	205
Pap et al. (1991)	Disc-integrated plage area	BB	1986	125, TSI
Steinegger et al. (1996)	Disc-integrated plage area	SP	1980	TSI
Lean et al. (1998)	Disc-integrated plage area	BB	1991–1995	TSI, 120–420
Solanki & Fligge (1998)	Disc-integrated plage area	MW [(a)]	1915–1984	TSI
Foukal (2002)	Disc-integrated plage area	MW, SP	1915–1999	TSI
Ambelu et al. (2011)	Disc-integrated index	MW, SP [(b)]	1915–2009	TSI
Foukal (2012)	Disc-integrated plage area	MW, SP	1915–1999	TSI, 130–240
Morrill et al. (2011a)	Disc-integrated plage area	BB	1991–1995	140–410
Johannesson et al. (1995)	Disc-integrated intensity	BB	1991–1994	125
Chapman et al. (1996)	Disc-integrated intensity	SF	1988–1992	TSI
Johannesson et al. (1998)	Disc-integrated intensity	BB	1987–1996	125
Preminger et al. (2002)	Disc-integrated intensity	SF	1988–1996	TSI
Walton et al. (2003)	Disc-integrated intensity	SF	1989–1996	TSI
Vogler et al. (2005)	Disc-integrated intensity	ML	1999	TSI
Chapman et al. (2012)	Disc-integrated intensity	SF	2003–2010	TSI
Chapman et al. (2013)	Disc-integrated intensity	SF	1988–2010	TSI
Puiu (2019)	Disc-integrated intensity	RP	2000–2019	TSI
Choudhary et al. (2020)	Disc-integrated intensity	SF	2003–2018	TSI
Chatzistergos et al. (2020a)	Disc-integrated intensity	RP, SF	1996–2020	TSI
Worden et al. (2001)	Spatially resolved plage area	SP	1991–1996	120–170
Morrill (2005)	Spatially resolved plage area	BB	1991–1995	276–288
Morrill et al. (2011b)	Spatially resolved plage area	MW	1961–1981	276–288
Semi-empirical models				
Ermolli et al. (2003)	Spatially resolved plage area	RP	1996–2001	TSI
Penza et al. (2003)	Spatially resolved plage area	RP	1996–2001	TSI, 403, 501, 863
Ermolli et al. (2011)	Spatially resolved plage area	RP	1997–2010	TSI
Criscuoli et al. (2018)	Disc-integrated plage area	SF, ML	1988–2015	115–310
Fontenla & Landi (2018)	Spatially resolved plage area	Co, MD1, RP	2002–2016	TSI,100–100 000
This work	Spatially resolved filling factors	13 archives	1978–2019	TSI, 115–160 000

Notes. Columns are: Bibliographic entry, type of input data and Ca II K archive(s) used, period and wavelength range of the reconstructed irradiance with Ca II K data. The studies are separated into four groups based on the method used for the irradiance reconstruction: empirical regression models using time series of plage areas or Ca II K index; empirical regression models using time series of disc-integrated intensities; empirical models using time series of plage areas and actual spectra; semi-empirical models using synthesised spectra from radiative transfer codes. See Table 2 for most of the archive abbreviations, while Co, ML, and SP refer to the Coimbra, Mauna Loa (centred at the core of the Ca II K line in contrast to the MLW data from the same observatory used here, which were centred at the wing of the line), and Sacramento Peak solar observatories, respectively. [(a)]Solanki & Fligge (1998) used the facular index compiled by Fligge & Solanki (1998), which included the MW plage areas by Foukal (1998). [(b)]Ambelu et al. (2011) used disc-integrated 1Å Ca II K index from SP and not the spectroheliograms.

2. Model

To calculate solar irradiance variations, we employ the SATIRE model (Fligge et al. 2000; Krivova et al. 2003; Yeo et al. 2014, 2017b; Dasi-Espuig et al. 2016; Tagirov et al. 2019). SATIRE is a semi-empirical model. It takes the distribution of the solar surface magnetic features (sunspot umbrae and penumbrae, as well as faculae and the network) from solar observations. The brightness of these features is computed from the appropriate solar model atmospheres with the radiative transfer codes (Unruh et al. 1999; Norris et al. 2017; Tagirov et al. 2019). The model replicates more than 90% of the TSI variability measured from 1978 to the present (Yeo et al. 2014, 2017b).

There are different versions of the SATIRE model, depending on the input data and consequently the period covered by the reconstruction (Krivova et al. 2011). The ones of relevance for this paper are SATIRE-S, SATIRE-3D, SATIRE-T, and SATIRE-T2. SATIRE-S (for Satellite era; Krivova et al. 2003, 2009b; Wenzler et al. 2006; Ball et al. 2012; Yeo et al. 2014) and the most recent SATIRE-3D (Yeo et al. 2017b) use full-disc longitudinal magnetograms to derive facular coverage as a function of time and white-light observations for sunspots. Such data are available for the last four decades. SATIRE-T and -T2 (for Telescopic era) use sunspot observations (areas, sunspot number, group sunspot number) to infer the coverage by both

sunspots and faculae back to 1609 (Krivova et al. 2007, 2010; Dasi-Espuig et al. 2014, 2016; Wu et al. 2018).

We based our model on the SATIRE-S version (see Fligge et al. 2000; Krivova et al. 2003; Yeo et al. 2014). In SATIRE-S, irradiance variations are computed as the sum over the entire solar disc of the intensity spectra of each image pixel. Using the full-disc magnetograms and continuum images, each pixel is assigned in one of the four atmospheric components: sunspot umbra, penumbra, facula (including the network) and the quiet Sun (that is the surface free of any magnetic signal above the magnetogram noise threshold). We used the same intensity spectra as in all standard versions of SATIRE-S, and SATIRE-T/T2 (Wenzler et al. 2006; Ball et al. 2012; Yeo et al. 2014; Dasi-Espuig et al. 2016). (Different facular spectra were employed by Tagirov et al. 2019, who used facular spectra computed in non-LTE approximation to test non-LTE effects on the reconstruction of the UV irradiance and by Yeo et al. 2017b in the SATIRE-3D version, who used intensities computed from 3D MHD solar atmospheres.) The spectra we employ were computed with the ATLAS9 code (Kurucz 1970) by Unruh et al. (1999) from semi-empirical model atmospheres. The quiet Sun is represented by the Kurucz (1993, 2005) model at $T = 5777$ K, sunspot umbrae and penumbrae by the models with $T = 4500$ K and $T = 5450$ K, respectively and faculae and network by the FALP model (Fontenla et al. 1999) modified by Unruh et al. (1999).

Instead of direct solar magnetograms, which are only available for the last several decades and cannot be used for longer irradiance reconstructions, we used Ca II K images to derive the information on the distribution of the facular (plage) regions on the visible solar disc. For this, Ca II K observations were converted into unsigned longitudinal magnetograms (see Sect. 3), which provide information on the location on the disc and the magnetic field density in facular and network regions. From the reconstructed unsigned longitudinal magnetograms, we derived the facular filling factors (that is the fraction of a given pixel covered by a facular region) as done in SATIRE-S (see Yeo et al. 2014). This means that the filling factor of a given pixel, $a^{\rm f}_{ij}$, is proportional to the (radial) magnetic field density in that pixel, $|B_{r,ij}|$, until the saturation limit, $B_{\rm sat}$ is reached:

$$a^{\rm f}_{ij} = \begin{cases} |B_{r,ij}|/B_{\rm sat} & \text{if } |B_{r,ij}| < B_{\rm sat} \\ 1 & \text{if } |B_{r,ij}| \geq B_{\rm sat}, \end{cases}$$

where $B_{\rm sat}$ is the free parameter of the model. It accounts for the uncertainty in the exact relationship between the magnetic flux measured in the magnetograms (which depends on their spatial resolution, e.g., Krivova & Solanki 2004) and the true brightness of the corresponding magnetic region on the Sun (for further details, see Fligge et al. 2000; Yeo et al. 2014). (The SATIRE-3D version of the model uses 3D MHD solar atmosphere models to obtain this relationship for SDO/HMI magnetograms directly, Yeo et al. 2017b, but this approach is not possible when using Ca II K data, as the MHD simulations used for this purpose do not yet cover the heights at which the Ca II K line core is formed with sufficient accuracy.) To fix the value of $B_{\rm sat}$, we search for the value that returns the TSI reconstruction with the lowest RMS difference to a reference record of TSI measurements (see Sect. 3.2).

Sunspots cannot be adequately identified in the Ca II K data for the objective of our study. Therefore, to derive the filling factors of umbrae and penumbrae, $a^{u,p}_{ij}$, we used the sunspot area composite series by Mandal et al. (2020). This record of sunspot group observations had been compiled using historical data from various observatories covering the period 1874–2019, that is, the whole period over which Ca II K images are available. This database provides areas and μ positions of individual sunspot groups, but not for umbra and penumbra separately. We used a constant ratio of 0.25 for the umbra to penumbra area to separate between them (Solanki 2003; Wenzler et al. 2005). The filling factors of umbra and penumbra have the value of 1 in pixels belonging to these regions and 0 otherwise.

However, sunspots can be present in Ca II K observations too. Their appearance depends on the observational conditions and the bandwidth used for the observation (Chatzistergos et al. 2019b, 2020c). Mostly, their contrasts are either negative or very close to zero, but some parts might still appear bright in Ca II K. Since we get sunspot and facular information from different sources, it can happen that these bright sunspot patches are counted by us as faculae. Their overall fractional contribution is, however, minimal. In the following, unless otherwise stated, we assume that this effect can be neglected (cf. Sect. 4.2).

3. Data

In this work we employ observed full-disc Ca II K and red-continuum images as well as published time series of TSI plus sunspot area series.

3.1. Full-disc observations

We used full-disc Ca II K observations from the Baikal (Ba), Big Bear (BB), Brussels (Br), Calern (CL), Kanzelhöhe (Ka), Mees (MS), Meudon (taken with a spectroheliograph, MD1), Mt Wilson (MW), Rome (RP, taken with the Precision Solar Photometric Telescope, PSPT), San Fernando (SF, taken with the Cartesian Full-Disk telescope 2, CFDT2), and Teide (Te, taken with the Chromospheric Telescope, Chrotel) observatories. We also used observations taken in the line-wings (hereafter referred to as off-band) from Meudon and Mauna Loa (taken with the PSPT). In particular, we used observations from the Mauna Loa solar observatory centred at 3936.3 Å (MLW) as well as Meudon observations centred at 3932.3 Å (MDW, in the blue wing of the line). Table 2 lists the main characteristics of the analysed data.

The 13 archives considered in this study describe the main characteristics of the various available Ca II K series. The full-disc Ca II K observations have been taken with a spectroheliograph (MD1, MDW, and MW) or an interference filter (Ba, BB, Br, CL, Ka, MLW, MS, RP, SF, and Te). There are data taken exclusively with a CCD camera (Ba, BB, Br, CL, Ka, MDW[1], MLW, MS, RP, SF, and Te) or stored on photographic plates (MW), while MD1 includes both. The analysed archives cover the full range of employed bandwidths at the various sites, with SF and MD1 using the broadest and narrowest ones, respectively. We also tested CCD data with small (e.g., RP or Te) and large (e.g., MS or BB) pixel scales. We note that for MD1 we analysed newly digitised data over 1982 and 1997–2002. This was because many photographic plates from older digitisation over these two periods were found to exhibit saturated regions. This was because many photographic plates from the former digitisation over that period were found to exhibit saturated regions (Chatzistergos et al. 2019b), which limit the applicability of those data for TSI reconstructions.

The Ca II K data used here encompass 63 691 images covering 13 372 days over the period 1978–2019. Since the main aim of this work is to develop and test a method for the irradiance

[1] MDW also has data stored on photographic plates; however, here we restricted our analysis to the CCD-based data.

Table 2. Ca II K datasets analysed in this study.

Observatory	Acronym	Detector	Instrument	Period	Images	WL [Å]	SW [Å]	Pixel scale [″/pixel]	Refs.	Figs.
Baikal	Ba	CCD	Filter	2004–2019	789	3933.7	1.2	2.7	1	6
Big Bear	BB	CCD	Filter	1982–2006	5026	3933.7	3.2, 1.5 [(a)]	4.2, 2.4 [(b)]	2	8
Brussels	Br	CCD	Filter	2012–2019	13248	3933.7	2.7	1.0	3	6
Calern	CL	CCD	Filter	2011–2019	1501	3933.7	7	1.0	4	6
Kanzelhöhe	Ka	CCD	Filter	2012–2019	4146	3933.7	3.0	1.0	5	8
Mauna Loa PSPT	MLW	CCD	Filter	2004–2015	9552	3936.3	1.0	1.0	6	7
Mees	MS	CCD	Filter	1988–1998	1513	3933.7	0.3 [(c)]	5.5	7	6
Meudon	MD1	Plate/CCD [(d)]	SHG	1978–2019	11916	3933.7	0.15, 0.09 [(e)]	2.2, 1.5, 1.1 [(f)]	8	10
....	MDW	CCD	SHG	2002–2018	4481	3932.3	0.15	1.5	8	7
Mount Wilson	MW	Plate	SHG	1978–1985	2413	3933.7	0.2	2.9	9	10
Rome PSPT	RP	CCD	Filter	1996–2019	3337	3933.7	2.5	2.0	10	2
San Fernando CFDT2	SF	CCD	Filter	1992–2013	4061	3933.7	9	2.6	11	6
Teide ChroTel	Te	CCD	Filter	2009–2019	1708	3933.7	0.3	1.0	12	6

Notes. Columns are: name of the observatory, abbreviation used in this study to refer to this dataset, type of detector, type of instrument, period of observations, total number of analysed images, central wavelength and spectral width of the spectrograph or filter, average pixel scale of the images, the bibliography entry, and the figure number in this paper showing the reconstructed TSI series with that dataset. [(a)]The two values correspond to the period before and after 10 September 1996, when the filter was changed. [(b)]The two values correspond to the period before and after 08 November 1995, when the CCD camera was upgraded. [(c)]This dataset comprises observations taken with an adjustable Lyot filter, and the main settings for bandwidth and offset in the central wavelength should be 0.3 Å and 0 Å, respectively. However, it is likely that it includes observations with the following settings too: [1.2, 0] Å, [0.3, −0.6] Å, [0.6, −0.6] Å for bandwidth and central wavelength combinations, respectively. [(d)]The observations were stored on photographic plates up to 27 September 2002, while observations with a CCD camera started on 13 May 2002. [(e)]The values refer to the periods [01 January 1978–14 June 2017] and [14 June 2017–31 December 2019]. [(f)]The values refer to the periods [01 January 1978–27 September 2002], [28 September 2002–14 June 2017], and [15 June 2017–31 December 2019].
References. (1) Golovko et al. (2002); (2) Naqvi et al. (2010); (3) http://www.sidc.be/uset/; (4) Meftah et al. (2018); (5) Hirtenfellner-Polanec et al. (2011); (6) Rast et al. (2008); (7) http://kopiko.ifa.hawaii.edu/Reference/KLINE/; (8) Malherbe & Dalmasse (2019); (9) Lefebvre et al. (2005); (10) Ermolli et al. (2007); (11) Chapman et al. (1997); (12) Bethge et al. (2011).

reconstruction from Ca II K data, here we restrict the analysed period to that of the direct TSI measurements, that is since 1978. The analysis by Chatzistergos et al. (2020c) of the same archives over the considered period includes 73 819 images. However, for 414 days (mainly over 2018–2019), the series by Mandal et al. (2020, see Sect. 2) does not have information on the sunspot areas and hence we cannot use the Ca II K observations on these days for the irradiance reconstructions. The archives in general include a varying number of observations per day, with most observatories aiming at acquiring roughly 1–3 Ca II K images per day. However, some observatories also carry flare patrol campaigns in Hα line, which require a greater amount of data taken with shorter cadence, typically of a few seconds to minutes, and complement those with similarly high-cadence Ca II K observations. That is the case for the Ba, Br, CL, Ka, and Te archives. We analysed all available observations from Br. For Ba, CL, Ka, and Te we either analysed the 'best' observation per day as identified by the observers, for the case of Ba, or randomly selected two to three images devoid of artefacts due to clouds (for more information, see Chatzistergos et al. 2020c). We did one exception for the first week of June 2014, for which we analysed all available observations from all datasets used here in order to test the influence of seeing on our results (see Sect. 5.4). Over the analysed period, the high-cadence archives provide up to 18 and 868 images per day (for Ba and Br, respectively).

We process the Ca II K images with the methods described by Chatzistergos et al. (2018b, 2019b, 2020c) to perform the photometric calibration (only for the historical data) and compensate for the limb-darkening and any large-scale intensity pattern, thus creating contrast images. All images have been processed in a consistent manner.

We convert the Ca II K observations from all archives to unsigned longitudinal magnetograms with the relation determined by Chatzistergos et al. (2019d). We note that this process returns SDO/HMI-like magnetograms because the relation was determined for SDO/HMI (Helioseismic and Magnetic Imager aboard the Solar Dynamics Observatory; Scherrer et al. 2012; Schou et al. 2012; Pesnell et al. 2012) magnetograms. Therefore, some differences are expected between our reconstructed magnetograms and those obtained from sources other than SDO/HMI. Since this relation was derived for RP data, to apply it on observations from other archives we normalised the standard deviation of the quiet Sun regions to the average value found for RP data. In Fig. 1 we compare histograms of the unsigned radial magnetic flux density $|B_r|$ on 11 August 2001 (top panel), 16 July 2009 (middle panel), and 10 May 2012 (bottom panel) for the magnetograms reconstructed from RP, MD1, and SF datasets as well as the SDO/HMI magnetogram (shown only in the bottom panel as HMI data are not available prior to 2010). All images were first resized to the same dimensions. We also show the histograms for the magnetograms reconstructed from Ca II K images without their normalisation to the RP quiet Sun contrast. The normalisation improves considerably the agreement with the RP data. The histogram for the SDO/HMI magnetogram on 10 May 2012 is very close to the histograms for the reconstructed magnetograms after normalising them to RP data. We note that the $3-\sigma$ noise level of the 315-second SDO/HMI magnetograms is ~20 G (Yeo et al. 2013, 2014), which explains the difference at lower $|B_r|$ values.

However, we also notice some mismatch, mostly at high $|B_r|$ values, potentially hinting at a non-linear relation of the normalisation factors between archives. We do not expect the mismatch over high $|B_r|$ values to be important for our analysis here since the free parameter of the model $B_{\rm sat}$ would account for this. But a forthcoming study will address this issue in more detail.

To test the effect of sunspot identification (Sect. 4.2), we also analyse full-disc RP observations taken in the red continuum at 607.1 nm with a bandwidth of 0.5 nm covering the period

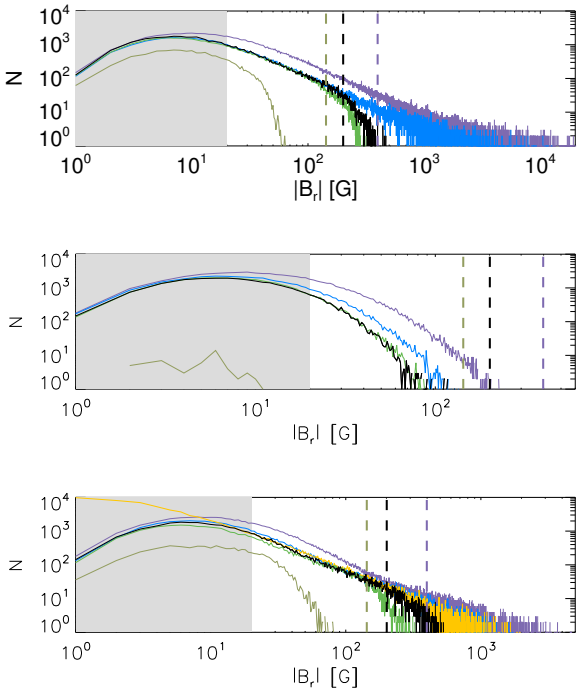

Fig. 1. Histograms of the unsigned radial magnetic flux density $|B_r|$ in magnetograms reconstructed from Ca II K observations taken on 11 August 2001 (*top*), 16 July 2009 (*middle*), and 10 May 2012 (*bottom*). The observations used are from RP (black), MD1 (blue/purple for reconstructions with/without the normalisation of the contrast values to RP, see Sect. 3), SF (dark/light green for reconstructions with/without the normalisation), and SDO/HMI (orange, shown only in the bottom panel as these data are not available prior to 2010) archives. The histograms are produced for bins of 1 G. The vertical dashed lines mark the adopted $B_{\rm sat}$ value for each archive when using PMOD TSI as the reference, while the grey shaded surface denotes the 3-σ noise level (~20 G) of the SDO/HMI magnetograms.

1997–2019. These images were processed in the same way as Ca II K images to compensate for the limb-darkening and large-scale intensity patterns affecting the observations (Chatzistergos et al. 2020a).

3.2. TSI series

To constrain the free parameter of the model and to test the accuracy of our reconstructions, we also used three records of direct TSI measurements from individual instruments, four TSI composites of measurements, and 7 irradiance series produced with models.

In particular, we used the TSI measurements from the Total Irradiance Monitor (TIM) on board the SOlar Radiation and Climate Experiment[2] (SORCE, version 19, February 2020 both for daily averages and 50 s cadence data; Kopp et al. 2005), TSI Continuity Transfer Experiment[2] (TCTE/TIM, version 4 for 50 s cadence data; Kopp et al. 2013), and Variability of solar IRadiance and Gravity Oscillations (VIRGO) experiment on board the SOlar and Heliospheric Observatory[3] (SOHO, version 6.5, May 2018 for daily averages and version created on 09 June 2016 for 60 s cadence data series; Fröhlich et al. 1997) instruments. We note that the daily values were used to constrain the free parameter, while the high-cadence data were used only to compare to our reconstruction.

The composite TSI series used are the ACRIM[4] (Active Cavity Radiometer Irradiance Monitor, which is the instrument taken as the reference by Willson 1997; Willson & Mordvinov 2003, version 30 November 2013), PMOD[3] (named after Physikalisch-Meteorologisches Observatorium Davos; version 42.65 15 July 2018; Fröhlich 2006), RMIB[5] (named after Royal Meteorological Institute of Belgium, in French called IRMB, version downloaded on 17 August 2020; Dewitte et al. 2004; Dewitte & Nevens 2016), and the one by Gueymard (2018, GEA18, hereafter). The ACRIM, PMOD, and RMIB composites are created with a daisy-chain process of using the measurements of one instrument as the reference to calibrate the counts of a second one, which then would act as the reference for another instrument. A value provided on a given day is an average over all measurements on that day by a single instrument. We note that the ACRIM TSI composite series has not been updated since 2013, but it is used here for completeness.

For comparison we also used seven irradiance series produced with models. These are the TSI reconstructions with the SATIRE-S[6] (Yeo et al. 2014, covering 23 August 1974–21 June 2019), SATIRE-T[6] (Wu et al. 2018, covering 2 July 1643–31 May 2017), SATIRE-T2[6] (Dasi-Espuig et al. 2016, covering 3 January 1700–7 November 2008), the NRLTSI[2] (Naval Research Laboratory TSI, covering 1 January 1882–31 December 2020; Coddington et al. 2016), the EMPIRE[6] (EMPirical Irradiance REconstruction, covering 14 February 1947–31 May 2017; Yeo et al. 2017a), NN-SIM[2] (Neural Network for Solar Irradiance Modeling, covering 08 November 1978–31 March 2019; Mauceri et al. 2019), and the Chatzistergos et al. (2020a, PSUM, hereafter, for Photometric SUMs, covering 16 May 1996–12 June 2020)[6] model. The methodology of SATIRE-S, SATIRE-T, and SATIRE-T2 is described in detail in Sect. 2. The remaining models apply linear regressions between solar activity proxies and measurements of solar irradiance. NRLTSI and EMPIRE both used the Mg II index for the facular contribution for the period discussed in this work, but differ in that NRLTSI applied ordinary least squares regression, while EMPIRE used orthogonal distance regression. NN-SIM reconstructed irradiance using artificial neural networks fed with 6 solar proxies: Mg II index, Lyman α irradiance at 121.6 nm, photometric sunspot index, and radio flux at 10.7, 15, and 30 cm. The series by Chatzistergos et al. (2020a) used the photometric sum indices computed from RP Ca II K and blue continuum observations for the regression, following Chapman et al. (2013).

4. Results for RP observations

In this section, we present and discuss the TSI reconstruction from the RP data, which is the longest and most consistent modern archive of high-quality Ca II K observations. Results for other archives are presented in Sect. 5.

4.1. Irradiance reconstruction and the effect of the reference TSI series

Figure 2 shows the TSI reconstructed from the RP images with the PMOD TSI series used as the reference to set $B_{\rm sat}$. The model

[2] Available at the LISIRD archive at lasp.colorado.edu/lisird/
[3] Available at https://www.pmodwrc.ch
[4] Available at https://web.archive.org/web/20170611210135/http://acrim.com/
[5] Available at ftp://gerb.oma.be/steven/RMIB_TSI_composite/
[6] Available at http://www2.mps.mpg.de/projects/sun-climate/data.html

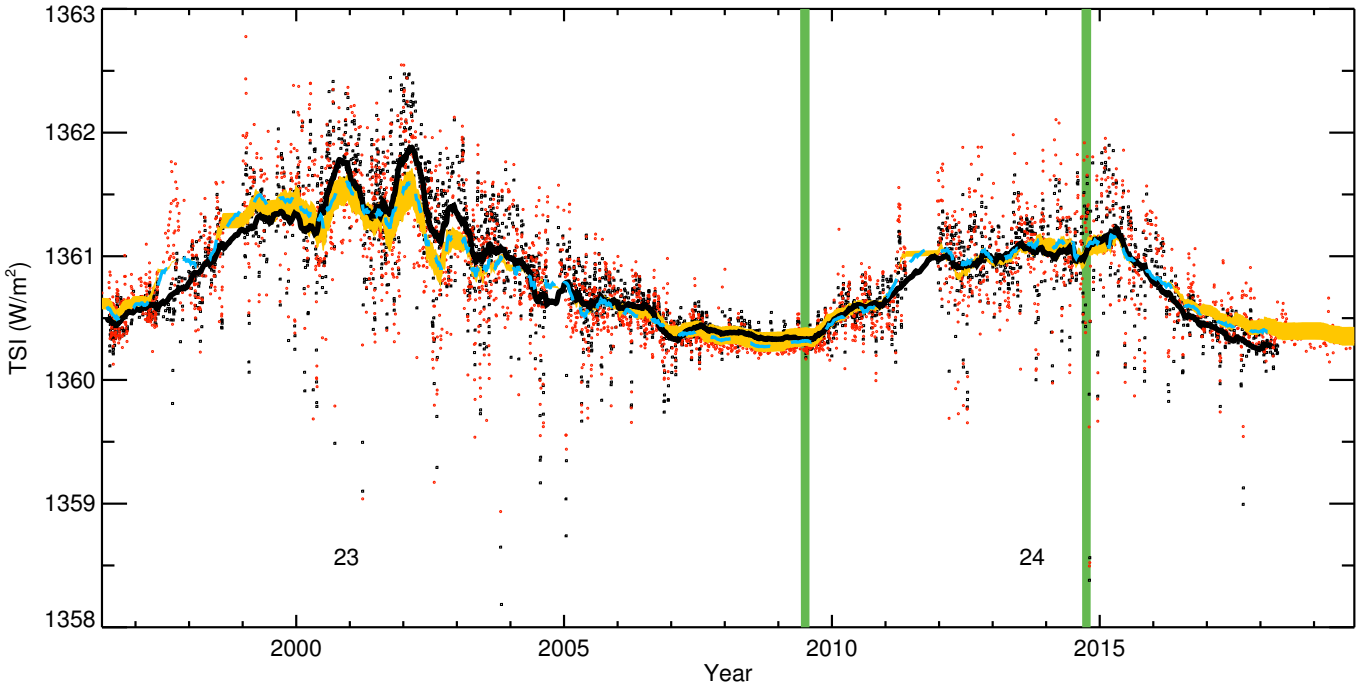

Fig. 2. TSI reconstructed with RP Ca II K data (red circles for daily values and light blue dashed line for 81-day running mean values) using the PMOD TSI series as the reference as a function of time. Also shown is the PMOD TSI composite (black squares for daily values and black solid line for 81-day running mean values). The orange shading shows the range of the TSI reconstructions (81-day running means) obtained with the minimum and maximum B_{sat} value determined from all reference TSI series considered here (see Table 3). The numbers underneath the curves denote the solar cycle numbers, while the green vertical bars mark the intervals shown in Fig. 3. The running means are produced by considering only the days on which both series are available.

and the PMOD record are in good agreement with each other. Pearson's linear correlation coefficient, R, and the RMS difference over the whole period are 0.91 and 0.21 Wm^{-2}, respectively. For comparison, the correlation coefficient and the RMS difference between the PMOD and SATIRE-S over the same period are 0.98 and 0.16 Wm^{-2}, respectively. To better illustrate the agreement between the two models and the PMOD record on shorter timescales, in Fig. 3 we also show the TSI changes over two 2-month periods close to the activity maximum (June–July 2001) and minimum (June–July 2009). While the Ca II K-based reconstruction appears slightly noisier than SATIRE-S relying on space-based magnetograms, it still does an excellent job.

It has already been shown earlier (Wenzler et al. 2009; Krivova et al. 2009a; Yeo et al. 2014; Chatzistergos et al. 2021) that the choice of the TSI reference record does not significantly affect the value of the free parameter, B_{sat}, and thus the final reconstructions. Here, we nevertheless tested this again. In particular, we used four TSI composites (PMOD, ACRIM, RMIB, and GEA18), two individual instrumental records (SOHO/VIRGO and SORCE/TIM), as well as seven alternative TSI models (SATIRE-S, SATIRE-T, SATIRE-T2, EMPIRE, NN-SIM, NRLTSI and PSUM) as references (see Sect. 3.2 for the description of these data). Table 3 lists the resulting B_{sat} values together with the corresponding R and RMS for these various reconstructions. In particular, the best agreement with PMOD is reached with B_{sat} = 201 G. This value is roughly in the middle of the entire range of 188–212 G obtained for all reference series of direct TSI measurements considered here. The RMS differences between the reconstruction with B_{sat} = 201 G and those with the two extreme cases of B_{sat} are 0.043 and 0.010 Wm^{-2}, respectively. Somewhat higher values of B_{sat}, 238 and 263 G, are obtained when using the SATIRE-T and SATIRE-T2 models, respectively. These somewhat higher deviations are attributed to the concept of those two models. They rely on sunspot observations alone and are less accurate on timescales of days to a few years (Krivova et al. 2009a).

Nevertheless, employment of all the records listed in Table 3 as the reference results in very similar TSI reconstructions (see Appendix A). This is also demonstrated in Figs. 2 and 3 by the shaded area, which marks the entire range of the reconstructed TSI values. The value of B_{sat} affects mainly the amplitude of the cycle variation, with higher values of B_{sat} returning weaker cycle amplitudes. The long-term trend is, however, barely affected by the selection of B_{sat} within the range of values derived with the various reference series (see also Chatzistergos et al. 2021). The correlation coefficient, R, is ∼0.9 or higher, while the RMS stays below 0.25 Wm^{-2} in all cases. The only exception for the direct TSI series is the ACRIM composite, with which the agreement is clearly poorer (R = 0.81 and RMS = 0.35).

In summary, the TSI reconstructed from the RP data is in excellent agreement with the published TSI series (except ACRIM), and the result is essentially independent of the series employed as the reference record to determine the free parameter.

4.2. Contribution of sunspots to facular filling factors

As mentioned in Sect. 2, sunspots can also partly appear as bright regions in Ca II K observations. Since we derive sunspot and facular filling factors from different sources, we might count some sunspot regions as faculae. To check the potential effect of the miscounted sunspots on the model outcome, we performed and compared the following three runs:

(1) The sunspot series by Mandal et al. (2020), which gives the μ values of the sunspot groups but not their exact locations,

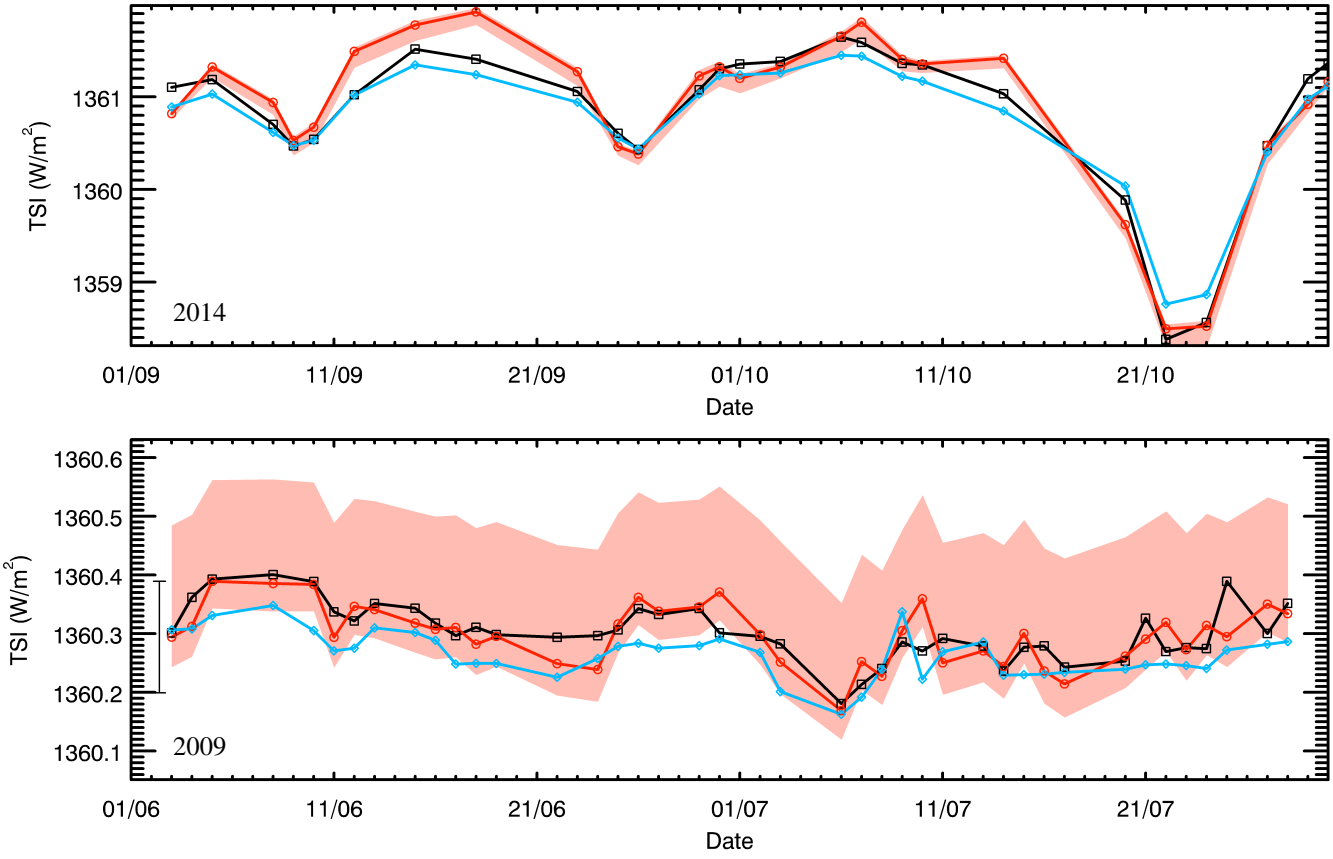

Fig. 3. TSI reconstructed from RP Ca II K data (red circles for daily values connected by the red line) during 2-month periods September–October 2014 (close to activity maximum, *top panel*) and June–July 2009 (around activity minimum, *bottom panel*). Also shown are the PMOD TSI composite (black squares and black curve) and the SATIRE-S TSI series (light blue diamonds and line). All series are only shown on the days when RP observations are available. The red shaded area shows the entire range of TSI obtained from RP Ca II K data using different reference series. We note that the range of TSI values shown in the two panels differs. To ease the comparison, the error bar in the lower panel marks the maximum range of the red shaded surface over the 2-month interval in 2014 shown in the top panel.

was used to compute the filling factors of sunspots (this is the approach used in Sects. 4.1 and 5);

(2) The series by Mandal et al. (2020) was used to compute the filling factors of sunspots, which were then subtracted from the facular filling factors for the same μ positions;

(3) The RP red-continuum observations were used to identify sunspots and derive their filling factors and positions, while these exact locations of sunspots were then used to block these regions in the Ca II K observations before computing facular filling factors. The first two cases make the extreme assumptions that sunspots either do not appear as brightenings in Ca II K data at all (case 1) or that they are always seen (case 2). Case 3 is the most accurate case, as we take exact positions and areas of spots into account.

Figure 4 shows the TSI reconstructed from RP with these different approaches to account for the sunspots, while scatter plots of these reconstructions versus the PMOD composite are shown in Fig. 5. All reconstructions are remarkably similar, and the effect of the 3 different approaches to account for sunspots on the resulting TSI is clearly minor. In particular, while the RMS differences (R) between the reconstructed series and PMOD TSI series is 0.20 Wm^{-2} (0.92) when using the RP red-continuum observations, the values are 0.21 Wm^{-2} (0.92) in both cases when we used the series by Mandal et al. (2020). These results remain qualitatively unchanged even if Ca II K datasets taken with different bandwidths are considered (see Appendix B).

These results suggest that the simplest approach of using the sunspot area series and the facular filling factors derived from Ca II K observations without correcting for the visibility of spots in the Ca II K data is entirely adequate to our purpose. This is important for historical irradiance reconstructions, because this approach can be used even with Ca II K data for which we do not have co-temporal continuum observations.

5. Towards TSI reconstructions from historical Ca II K archives

In the previous section we have shown that on modern high-quality Ca II K observations, our model works very well, reproducing $\gtrsim$85% of the measured TSI variations. This brings us one step closer to a reconstruction of the historical solar irradiance variability using Ca II K images to obtain facular coverage. Unfortunately, historical Ca II K observations have a lower quality than the RP data and suffer from various issues. While our method (Chatzistergos 2017; Chatzistergos et al. 2018b, 2019b, 2020c) allows for resolving many of these issues, the quality of such data remains poorer than that of RP images. Therefore, additional work will be needed to allow a reliable irradiance reconstruction back to the late 19th century. Here, we discuss such issues and their potential effect on the reconstructions. We start by considering the effect of the pixel scale of observations on the results (Sect. 5.1). Another critical issue is that

Table 3. Comparison of TSI reconstructions from different Ca II K series (columns) to various TSI reference sets (rows).

		(1)	(2)			(3)			(4)	
		RP	Te	Ba	MS	Br	CL	SF	MDW	MLW
PMOD	B_{sat} [G]	201	352	196	323	200	117	143	61	185
	RMS [Wm^{-2}]	0.21	0.27	0.24	0.32	0.21	0.28	0.28	0.26	0.18
	R	0.91	0.78	0.79	0.80	0.89	0.83	0.84	0.82	0.90
ACRIM	B_{sat} [G]	188	427	254	393	291	198	139	64	216
	RMS [Wm^{-2}]	0.35	0.33	0.28	0.40	0.30	0.36	0.39	0.33	0.24
	R	0.81	0.48	0.58	0.63	0.53	0.58	0.73	0.63	0.65
RMIB	B_{sat} [G]	205	361	198	339	212	122	143	63	189
	RMS [Wm^{-2}]	0.23	0.27	0.23	0.33	0.19	0.27	0.29	0.26	0.18
	R	0.90	0.78	0.80	0.78	0.89	0.83	0.84	0.81	0.89
GEA18	B_{sat} [G]	207	344	190	320	230	134	146	57	167
	RMS [Wm^{-2}]	0.23	0.26	0.29	0.33	0.21	0.29	0.28	0.26	0.20
	R	0.90	0.81	0.74	0.78	0.86	0.81	0.83	0.83	0.90
SOHO/VIRGO	B_{sat} [G]	200	353	197	476	200	117	141	61	185
	RMS [Wm^{-2}]	0.22	0.28	0.25	0.16	0.22	0.29	0.29	0.26	0.19
	R	0.91	0.78	0.78	0.83	0.88	0.82	0.84	0.82	0.89
SORCE/TIM	B_{sat} [G]	212	321	183	–	200	110	143	60	157
	RMS [Wm^{-2}]	0.17	0.26	0.26	–	0.18	0.27	0.20	0.24	0.18
	R	0.91	0.82	0.78	–	0.90	0.83	0.88	0.84	0.91
SATIRE-S	B_{sat} [G]	202	349	189	297	207	109	145	63	182
	RMS [Wm^{-2}]	0.20	0.25	0.22	0.37	0.18	0.29	0.30	0.26	0.19
	R	0.92	0.80	0.81	0.74	0.91	0.82	0.81	0.81	0.89
SATIRE-T	B_{sat} [G]	238	493	260	396	328	203	165	70	213
	RMS [Wm^{-2}]	0.34	0.35	0.32	0.46	0.32	0.36	0.39	0.35	0.27
	R	0.72	0.53	0.50	0.48	0.55	0.66	0.65	0.61	0.71
SATIRE-T2	B_{sat} [G]	263	–	–	332	–	–	189	43	142
	RMS [Wm^{-2}]	0.33	–	–	0.41	–	–	0.37	0.33	0.19
	R	0.76	–	–	0.70	–	–	0.68	0.77	0.77
EMPIRE	B_{sat} [G]	188	310	164	297	174	103	137	50	152
	RMS [Wm^{-2}]	0.25	0.30	0.30	0.37	0.24	0.33	0.31	0.27	0.21
	R	0.90	0.78	0.76	0.77	0.85	0.77	0.82	0.84	0.90
NRLTSI	B_{sat} [G]	202	319	173	312	181	100	144	57	159
	RMS [Wm^{-2}]	0.24	0.28	0.28	0.37	0.21	0.32	0.30	0.27	0.21
	R	0.89	0.79	0.76	0.76	0.89	0.78	0.82	0.82	0.89
NN-SIM	B_{sat} [G]	213	331	181	332	185	107	153	57	162
	RMS [Wm^{-2}]	0.23	0.30	0.29	0.35	0.23	0.34	0.30	0.27	0.21
	R	0.88	0.75	0.73	0.75	0.87	0.76	0.80	0.82	0.88
PSUM	B_{sat} [G]	204	320	172	492	185	100	142	58	168
	RMS [Wm^{-2}]	0.21	0.23	0.23	0.19	0.17	0.25	0.29	0.28	0.19
	R	0.91	0.86	0.83	0.76	0.93	0.86	0.83	0.80	0.89
MD1	B_{sat} [G]	194	417	222	321	260	145	133	74	214
	RMS [Wm^{-2}]	0.28	0.19	0.14	0.35	0.13	0.23	0.35	0.21	0.19
	RMS* [Wm^{-2}]	0.22	0.28	0.25	0.33	0.24	0.29	0.29	0.27	0.20
	R	0.87	0.86	0.92	0.80	0.94	0.86	0.80	0.85	0.84
	R*	0.92	0.74	0.77	0.80	0.83	0.80	0.85	0.79	0.86

Notes. The Ca II K series are divided into four groups: (1) RP (Sect. 4.1); (2) datasets employing a narrower bandwidth than RP (Sect. 5.2); (3) datasets employing a broader bandwidth than RP (Sect. 5.2); (4) datasets that have off-band observations (Sect. 5.2). The bottom section of the table shows the results when the reference dataset is, itself, the reconstruction from the MD1 Ca II K archive (see Sect. 5.6 for details). In this case, we also show the results of a comparison of the respective reconstruction to the PMOD TSI composite, marked with an asterisk in the table. The cells for the RMS differences are colour-coded from white to dark grey in the ranges [0, 0.2], [0.2, 0.3], [0.3, 0.4], [0.4, 0.5] Wm^{-2}.

observations have been taken with different bandwidths or even off-band (Sect. 5.2). We also consider the effects of instrumental changes (Sect. 5.3) and of varying or poor seeing (Sect. 5.4) on the reconstructions. Finally, we show two examples of reconstructions from photographic archives (Sect. 5.5) and discuss the possibility of using such a reconstructed series, in turn, as a reference for reconstructions from other archives (Sect. 5.6).

5.1. Effect of the pixel scale of the observations

Observations from different archives differ considerably in their pixel scale, ranging from 1 to 5.5″/pixel for the archives analysed here. To test whether the pixel scale affects our TSI reconstructions, we used the RP Ca II K data (with the original pixel scale of 2″/pixel) and performed eight TSI reconstructions by resizing

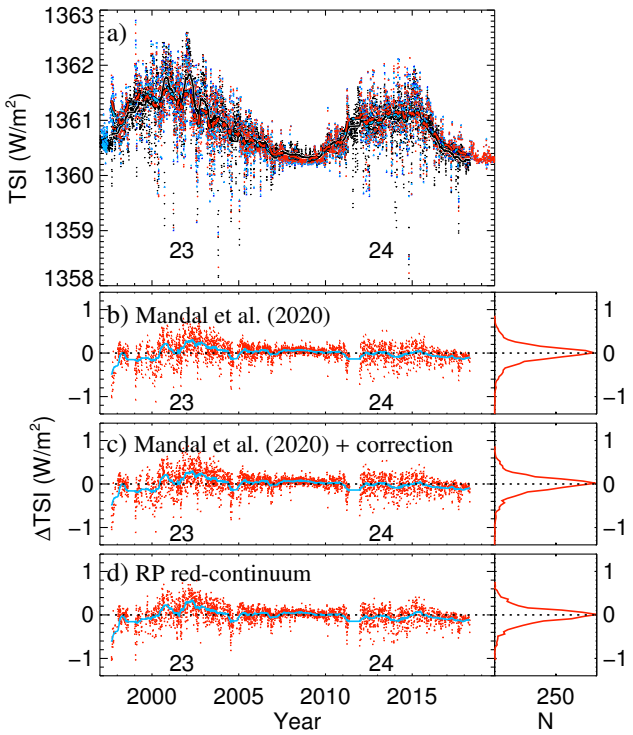

Fig. 4. TSI reconstructed from RP Ca II K data as a function of time (*a*) and difference of PMOD TSI composite to the TSI reconstructions (*b–d*) when using different approaches to account for sunspots: using the Mandal et al. (2020) series to get the sunspot filling factors (light blue in *panel a* and red in *panel b*); using the Mandal et al. (2020) series to get the sunspot filling factors, which are then subtracted from facular filling factors (blue in *panel a* and red in *panel c*); using full-disc Rome/PSPT red continuum data (red in *panels a and d*) to get the sunspot filling factors (see Sect. 4.2 for more information). The differences are shown only for the common days in all series. Also shown in *panel a* is the PMOD TSI composite (black). Thick lines show 81-day running mean values. The *right parts of the lower panels* show the distributions of the differences in bins of 0.05 Wm^{-2}. See Fig. 5 for the RMS differences between the various series as well as the correlation coefficient, *R*.

the observations such that the pixel scale ranged between 2.0 and 9.6″/pixel. We used the RP data, because of their quality, consistency and sufficiently long period of observations.

The reconstructions using the resized RP data are compared to that from the original RP data and to the PMOD TSI composite in Table 4. The value of B_{sat} grows somewhat with the increasing pixel scale from 201 G for the original-size data up to 248 G for the extreme case of 9.7″/pixel. The differences in the quality of the reconstructions between the various cases is essentially negligible for pixel scales up to 4.9″/pixel, while the quality is still rather good for a pixel scale of 9.7″/pixel. In particular, while the RMS difference between the resized and original reconstructions grows with the pixel scale, it remains low, with merely 0.081 Wm^{-2} for the pixel scale of 9.6″/pixel. Compared to PMOD, the RMS difference again changes very little for the resized data, reaching 0.223 Wm^{-2} for the pixel scale of 9.6″/pixel (0.214 Wm^{-2} for the reconstruction with the original RP data). This demonstrates that the pixel scale of the observations affects our results only weakly and suggests that data from archives with a large pixel scale, such as those from MS and BB, can also be used for irradiance reconstructions.

This is one of the big advantages of using Ca II K data compared to magnetograms. Due to the cancellation of opposite polarities, the magnetogram signal, and hence the amount of magnetic flux that is detected, drops rapidly with decreasing spatial resolution. Ca II K plage and the absolute magnetograms, including the absolute flux that are obtained from them, are far less sensitive to spatial resolution.

5.2. Effect of the bandpass of the observations

We now consider CCD data taken with filters with different bandpasses (see Table 2). Whereas Rome (RP) data were taken with a 2.5 Å wide filter, the data from Baikal (Ba), Mees (MS), and Teide (Te) were recorded with narrower filters in the range 0.3–1.2 Å. Broader filters with a width between 2.7 and 9 Å were used at Brussels (Br), Calern (CL), and San Fernando (SF). Figure 6 shows the reconstructed TSI from the above six Ca II K archives along with the PMOD TSI composite, while Table 3 lists the resulting B_{sat} values together with the corresponding *R* and RMS for the various reconstructions. We focus here on the case when PMOD is used as the reference. But for completeness, Table 3 also lists the cases when alternative reference records are used (as discussed in Sect. 4.1 for the example of RP reconstructions).

While the most accurate reconstruction is clearly achieved from the RP data, the agreement with the PMOD composite is good for all considered Ca II K archives. *R* is above 0.78 and the RMS difference is less than 0.32 Wm^{-2} for all considered datasets. Overall, the reconstructions from data taken with a broad or narrow bandwidth and their quality are all comparable. Some discrepancy between the TSI values in the reconstruction with MS data and the PMOD values in the early 1990s is due to scarcity of the data during that period, such that a meaningful comparison is difficult. Furthermore, the spectral bandwidth of the MS data was, in fact, not constant over the time, varying between 0.3 and 1.2 Å. Except MS, the highest RMS differences resulted from CL, SF, and Te data. SF and Te are the two extreme cases with respect to the employed bandwidth among the CCD-archives tested here, SF using the broadest and Te the narrowest bandwidth. The best estimate of B_{sat} generally increases with decreasing bandwidth employed for the Ca II K observations. In particular, the adopted B_{sat} value for RP data (201 G) is lower than that for Te data (352 G), which is consistent with the Te data having a narrower bandwidth, than the RP data.

To analyse the effect of the off-band observations on the irradiance reconstructions, we considered the data from Meudon (MDW) and Mauna Loa (MLW). Figure 7 and Table 3 present TSI reconstructions from these archives. These reconstructions are also in good agreement with the PMOD TSI series. But we again notice that the adopted B_{sat} generally decreases with the offset of the central wavelength of the observations from the line core. This might be due to the non-linearity of the relation between archives with different bandpasses (see Fig. 1 and Sect. 3.1), which will be addressed in a separate paper.

Overall, our preliminary analysis suggests that data taken with a narrower or broader passbands or offsets in the central wavelength can generally be used for historical reconstructions. Also noteworthy is that the accuracy of the reconstruction with the MS data is similar to that of the other archives (keeping in mind the scarcity of the observations), highlighting the value of even the archives with large pixel-scale for this purpose (see Sect. 5.1).

5.3. Uncertainties due to instrumental discontinuities

Another issue one has to deal with when using historical observations are changes in the instrumental setups with time. As an example, in Fig. 8 we show the TSI reconstructed from BB and Ka data, along with the PMOD TSI composite for comparison.

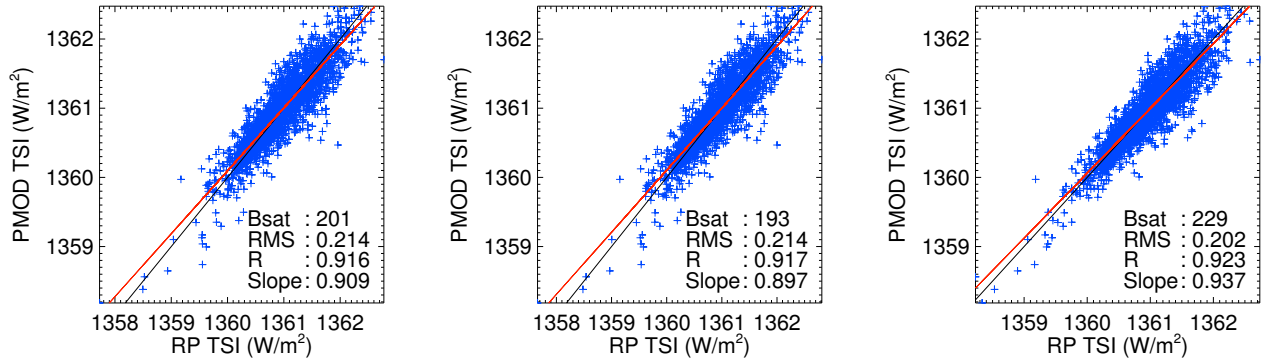

Fig. 5. TSI reconstructed from RP Ca II K images against the PMOD TSI composite. *Left:* sunspot information taken from Mandal et al. (2020) without any correction to the faculae filling factors due to sunspots; *middle:* sunspot information taken from Mandal et al. (2020) and the sunspot filling factors are subtracted from the facular ones; *right:* sunspot information is derived from the full-disc RP red-continuum images. The red lines show linear fits to the data, while the black lines have a slope of unity. Also listed in each panel are the B_{sat} (in G), RMS difference (in W m^{-2}), the linear correlation coefficient, and the slope of the linear fit.

Table 4. Comparison of TSI reconstructions from the resized RP Ca II K series to the PMOD TSI composite and the TSI reconstructions with original size RP data.

Pixel scale [″/pixel]	B_{sat} [G]	RMS [Wm^{-2}]		R	
		RP	PMOD	RP	PMOD
2.0	201	–	0.214		0.913
2.2	201	0.029	0.213	0.998	0.914
2.4	202	0.031	0.213	0.998	0.913
2.8	203	0.033	0.214	0.998	0.913
3.2	206	0.036	0.214	0.997	0.913
3.9	208	0.041	0.212	0.997	0.915
4.9	213	0.049	0.213	0.995	0.914
6.5	223	0.060	0.214	0.993	0.914
9.7	248	0.081	0.223	0.988	0.906

Both archives have known issues affecting consistency of their quality (Chatzistergos et al. 2020c).

The TSI series reconstructed from the BB data shows clear and abrupt changes, particularly evident in the difference between the PMOD TSI series and the reconstruction. These jumps coincide perfectly with the periods of instrumental changes (marked by vertical dashed lines in the figure). Most prominent is the jump on 7 July 2000, when a CCD calibration started being applied to the data. A possible exception is 10 September 1996 when the BB filter was replaced. At this time we do not see any abrupt change in the values compared to those from the PMOD series, although the scatter seems to decrease after the change.

The reconstruction from Ka data clearly deviates from PMOD TSI over 2011–2012, and the linear correlation drops down to 0.32 over this period. This coincides with the deterioration of the initial filter used at Ka, leading to a poorer quality of the images over this period. The filter was replaced on 24 November 2012. The results after the replacement of the filter at Ka are in excellent agreement with the PMOD TSI series.

These examples show the importance of understanding and knowing, as precisely as possible, any instrumental issues affecting the Ca II K datasets. If not properly accounted for, they will result in artefacts in the computed TSI. This also means that archives with such inconsistencies, which are not precisely accounted for, should be avoided when studying the long-term trend in solar irradiance. Furthermore, this points to the importance of using multiple archives whenever possible, which might help to identify inconsistency that would otherwise not be noticed.

5.4. Uncertainty due to sampling and seeing

The TSI reconstructions presented in the previous sections were daily mean values over all individual images (from a given archive) within a day. In this section, we discuss reconstructions from individual images from Ba, Br, CL, Ka, and Te datasets and compare them to the SOHO/VIRGO record with an hourly cadence as well as to SOHO/VIRGO, SORCE/TIM, and TCTE/TIM series with an approximately 1-min cadence. Figure 9a shows the reconstructed TSI over the course of the first week of June 2014. Panels b, c, and d are enlargements of panel a over 5 and 7 June 2014, as well as between 13:00 and 14:00 UTC on 7 June 2014, respectively. The variability within a given day is similar in the reconstructed TSI and in the measurements done with the 1-min cadence. The main sources of TSI fluctuations on these timescales are 5-min oscillations (Leighton et al. 1962) and granulation (see e.g., Shapiro et al. 2017), which we do not expect to see in Ca II K data.

Generally, on timescales of hours to a few days, the computed variability mimics that in the SOHO/VIRGO series, as can be seen for Ka over 7 June 2014 or Te over 5 June 2014. However, we sometimes also notice variations within a day with trends different from those in SOHO/VIRGO, for example for Te over 6 June 2014 or 7 June 2014. This is most probably the result of changing seeing conditions during the day at the Teide site.

For a more quantitative comparison, we remove roughly the effect of the evolution of magnetic features from all the reconstructed TSI series in the following way. We smooth the SoHO/VIRGO data having the 1-min cadence with a 30-min window and then subtract this smoothed series both from the original 1-min record and from all reconstructions. We then compute the standard deviations of these residual series within each day and list them in Table 5. For the considered first week of June 2014, the values for individual days and datasets lie in the range [0.03–0.18] Wm^{-2}. In particular, the values for the measurements lie between 0.05 and 0.11 Wm^{-2}, while those for the reconstructions between 0.03 and 0.18 Wm^{-2}. The values for the

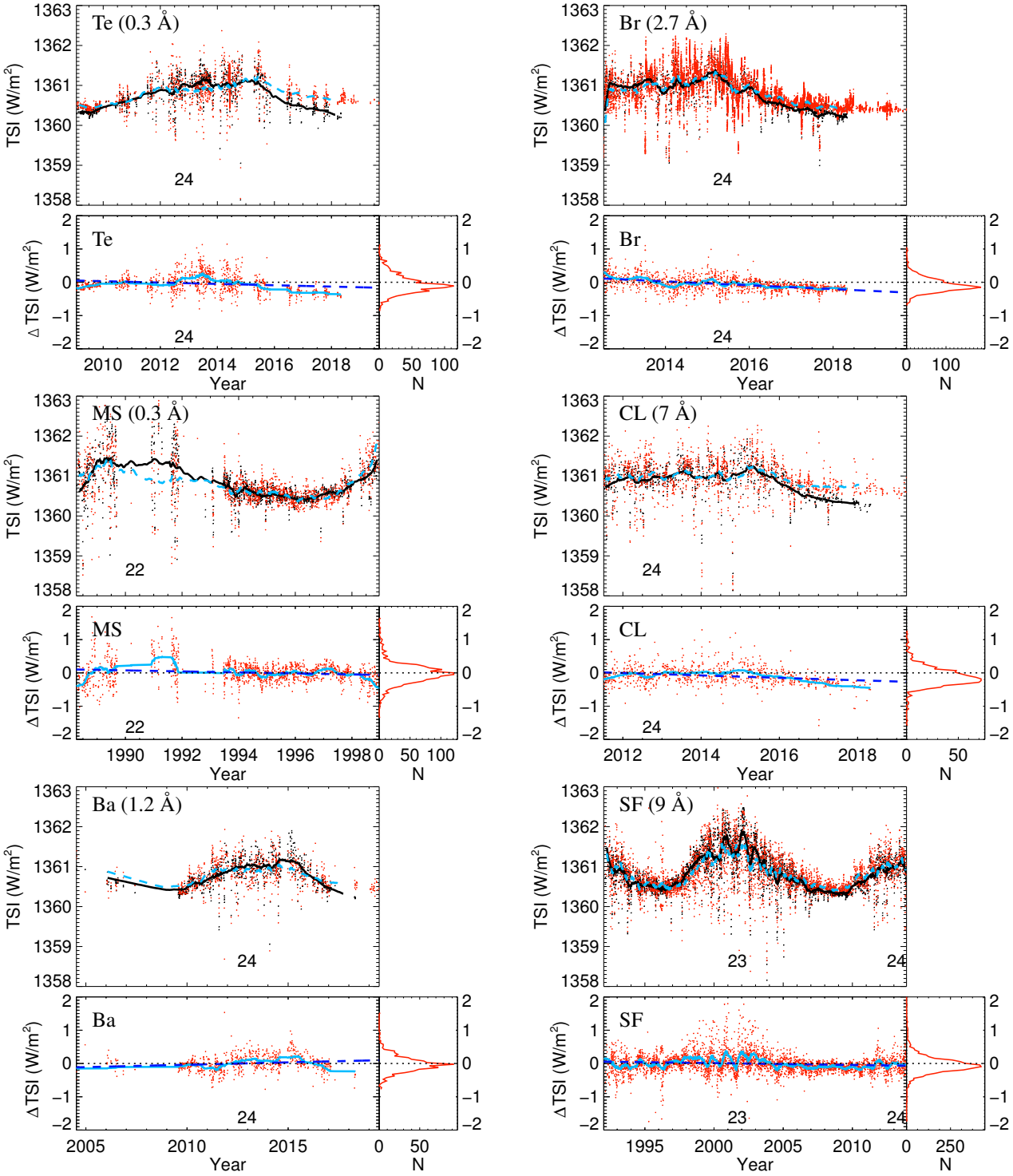

Fig. 6. *Upper part of each panel:* TSI reconstructions from Ca II K observations taken with filters that are narrower (*left column*) or broader (*right column*) than RP. Daily values from the Te, Br, MS, CL, Ba, and SF datasets are shown as red dots and the corresponding 81-day running means as dashed blue lines. For comparison, the PMOD irradiance composite series is overplotted (black dots for daily values and the solid black line for the 81-day running means). The running means have been computed considering only days on which both the reconstructions and the PMOD series were available. *Lower left part of each panel:* difference between the PMOD composite and the reconstructed TSI (red dots for daily values and solid light blue for 81-day running means). The dashed blue line is a linear fit to the residuals. The horizontal black dotted line marks the zero difference. *Lower right part of each panel:* distribution of the residuals in bins of 0.05 Wm^{-2}. The numbers at the bottom of each panel indicate the solar cycle number and are placed roughly around the maximum of the corresponding cycle.

reconstructions are generally comparable to those for the measurements, although with a tendency to be slightly higher. They also vary more from day to day than the values from the measurements. On 6 June, three of the four archives (Br, CL and Te) result in standard deviations more than twice higher than in the measurements (0.16–0.18 vs. 0.07 Wm^{-2}).

We consider these slightly higher values of the standard deviation as a very rough estimate of the uncertainty in the